

HiSST: 4th International Conference on High-Speed Vehicle Science Technology 22 -26 September 2025, Tours, France



High-Temperature Laser Probe for Optical Diagnostics in Supersonic Flows under Flow-Induced Vibrations

Ignacio Lasala¹, Lucas J. Ford¹, Eric Bach¹, Guillermo Paniagua¹, Etienne Choquet², Thierry Andre²

Abstract

A probe nacelle is designed to deliver a laser sheet for planar laser diagnostics in hightemperature supersonic flows subjected to flow-induced vibrations. The nacelle houses sheet-forming optics and submerges them directly into the flow field, improving modularity in facilities with limited external access. Placing the optics within the flow shortens the focal length of the optics and increases irradiance in the laser sheet, enhancing diagnostic capability. To withstand harsh operating conditions, the probe is equipped with an actively cooled jacket, enabling its use in high-temperature, high-pressure environments. A key challenge in these environments is vibration, which can disrupt optical alignment and focal positioning. This study demonstrates the ability of the probe to perform planar laser diagnostics under vibration by testing it in the Facility for Instrumentation and Open-Jet Research (FIOR) at PETAL laboratories. The probe was exposed to an 80-mm turbulent free jet operated at underexpanded supersonic conditions (Mach 1.15).

The flow through FIOR was seeded with micron-sized oil droplets and illuminated with the laser sheet for planar Mie scattering delivered by the probe. A high-speed camera, recording at 5-20 kHz, captured particle motion. Probe vibrations were measured with piezoelectric accelerometers sampled at 30 kHz and with high-speed optical imaging at 20 kHz, processed using Proper Orthogonal Decomposition (POD). It was found that the vibration amplitude of the probe increased linearly with jet momentum flux, reaching a maximum amplitude of 0.2 mm at Mach 1.15. Frequency analysis showed that accelerations were dominated by a 1600 Hz mode, while displacements were governed by a lowerfrequency 45 Hz mode. Planar Mie scattering was successfully conducted at the highest vibration levels, enabling visualization of flow structures within the particle-laden jet plume. An uninterrupted laser sheet was maintained under all test conditions. These results advance the development of actively cooled probe nacelles toward feasible laser sheet delivery withing supersonic environments, advancing diagnostic capabilities for high-Mach facilities.

Keywords: Vibration-resistant probe, laser probe, high-speed flow diagnostics, Mie scattering, Active cooling

Nomenclature

 C_n – Fourier coefficients

f – Frequency (or) focal length

FOV - Field of View

 \dot{m} – Mass flow

Latin

M - Mach number

P - Pressure

PDF – Probability Density Function

t - Time

T – Temperature

U - Velocity

x – Horizontal position

y – Vertical position

Greek

 ρ – Density

 σ – Standard deviation

Subscripts

0 - Total conditions

¹ Maurice J. Zucrow Laboratories, Purdue University, West Lafayette, IN, USA

² MBDA, Le Plessis Robinson, France

1 – Open jet exit conditions c – Coolant conditions 2 – Conditions downstream of bow shock p2p – Peak-to-peak

1. Introduction

High-fidelity measurements in supersonic, high-temperature flows depend on diagnostic tools resilient to harsh aerothermal environments. Traditional flow probes remain a robust and well-established method [1], [2], but their deployment in supersonic regimes requires careful aerodynamic and thermal design. These probes are exposed to severe thermal and mechanical loads, provide only pointwise measurements, and inherently disturb the local flow field. Internally liquid-cooled probes have been employed to survive high-temperature environments [3], [4], [5] and extensive literature exists on the geometric and aerodynamic design of probes for supersonic flows, where shock waves form near the body [2], [6].

Optical diagnostics, such as Mie-scattering, provide planar or volumetric flow visualization without distorting the flow. However, they require precise and often bulky optical access systems, which are frequently limited in high-Mach facilities due to structural constraints. [7], [8]. Placing laser-sheet forming optics directly within the flow shortens the focal length, improves irradiance, and allows modular placement of the laser beam or sheet without modifying facility walls [9]. Yet, in-flow optics face a major challenge: flow-induced vibration. Unsteady aerodynamic forces on immersed probes can misalign optics and shift focal planes [10], degrading data quality and repeatability. While throughwindow delivery avoids direct vibration exposure, it sacrifices flexibility and is limited by facility constrains.

This paper investigates a probe nacelle design as a versatile platform for in-flow optical diagnostics [9]. The nacelle can accommodate multiple optical configurations, enabling delivery of laser beams or sheets to regions of interest while protecting the optical train. By housing the optics within a rigid enclosure, relative alignment is preserved and sensitivity to flow-induced vibrations is reduced, as the optics are not directly exposed to aerodynamic forcing. An active cooling system allows the probe to operate in high temperature flows up to 1700 K [3], [4], but introduces additional vibrating energy whose impact needs to be considered and measured. To evaluate probe vibration performance, an open turbulent transonic flow is used to excite the nacelle. Vibrations are measured with piezoelectric accelerometers and high-speed optical imaging. Data are analyzed in both amplitude and frequency domains, providing a comprehensive characterization of the probe's dynamic response and correlating vibration behavior with flow momentum flux. The design allows different optical arrangements to be deployed while preserving alignment and improving signal quality, making it adaptable to diverse experimental needs. For demonstration, a single laser configuration for planar Mie scattering is integrated into the probe, and it has been successfully conducted in the open-jet flow to identify canonical flow structures. This represents a step toward the development of vibration-resistant, actively cooled probe nacelles capable of supporting modular laser diagnostics in supersonic facilities.

2. Methods

2.1. Probe Nacelle Geometry

The probe features a "ship's bow" leading edge to minimize the bow-shock angle while maintaining a parallel top surface to the freestream, thereby reducing disturbances above the probe. The angled front walls further deflect disturbed streamlines downward, mitigating perturbations in the region of interest. To withstand harsh conditions up to $T0=1700~\rm K$, the probe is 3D printed from Stainless Steel AISI 316 and incorporates an open-cycle gaseous cooling system surrounding the optical cavity. This system maintains surface temperatures below 810 K (the stainless-steel material limit) and constrains optical mounts and cage plates to below 315 K, the most restrictive limit dictated by motorized Thorlabs Inc. components. Cooling air is supplied through a plenum at the rear of the nacelle, routed around the optical cavity, and discharged via an array of effusion holes located at the front. Most cooling holes are oriented laterally rather than forward-facing, a configuration that reduces coolant interaction with the bow shock and lowers the required injection pressure as it does not need to exceed the stagnation pressure of the external flow to start ejecting. The probe dimensions are dictated by the modularity of interchangeable optical trains, with an optical cavity volume of 980 cm3, total length of 400 mm, height of 100 mm, and width of 86 mm. Further details on the geometry, aerodynamics, and

design philosophy can be found in Lasala et al. [9], where a comprehensive description is provided.

The main aerodynamic features around the probe, which guided its design, are schematized in Figure 1a. These features are visible in the CFD snapshot of Mach number contours shown in Figure 2b, taken from previous published work [9]. Figure 1c presents a section view of the probe, showing the optical cavity with two different optical arrangements: one delivering a single laser beam through the top window, and another introducing a laser sheet through the front. In this study, the latter configuration is employed to conduct planar Mie-scattering measurements in a free jet. In both cases, once the laser crosses the bow shock formed around the probe in supersonic conditions, the properties measured are the unaltered free stream properties of the flow.

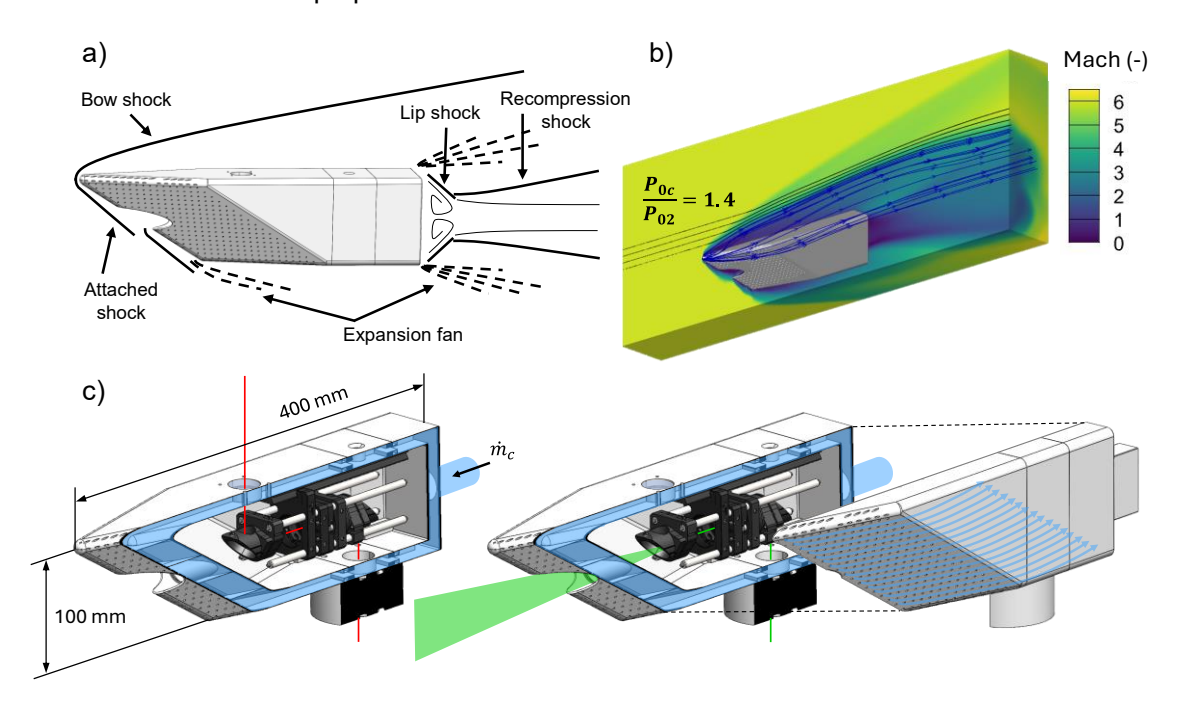


Figure 1: Probe nacelle with dominant aerodynamic features (a), Mach number contour from RANS CFD showing the effect of effusion cooling on the bow shock (b), and different optical arrangements for pointwise and planar laser diagnostics (c).

2.2. Wind Tunnel and Open Jet Test Section

The tests presented in this article were conducted at the Purdue Experimental Turbine Aerothermal Lab (PETAL) [11] using the Facility for Instrumentation and Open Jet Research (FIOR) fed by the pressure-driven wind tunnel Petal Tunnel 1 (PT1).

PT1 is a long-duration, pressure-driven wind tunnel capable of operating over a wide range of Reynolds and Mach numbers. It is fed by a 56 m³ dry air reservoir pressurized to 150 bar, discharging to ambient when the open test section (FIOR) is installed, or alternatively into a 283 m³ vacuum tank maintained at 10 mbar. The air supply passes through a natural gas-fired heat exchanger, delivering non-vitiated air at up to 600 K. Mass flow is measured with a calibrated venturi and purged until a fast-actuating butterfly valve initiates flow through the tunnel. A settling chamber with honeycomb and mesh screens homogenizes the flow before it reaches FIOR.

FIOR is a converging nozzle designed to deliver uniform, homogeneous flow at various Mach numbers and temperatures. It features an 80 mm exhaust diameter to allow the calibration and testing of large-scale probes such as the one presented in this article. The internal surface is shaped without inflection points to promote a thin boundary layer along the nozzle wall. The schematic of PT1 with the FIOR test section installed is shown in Figure 2.

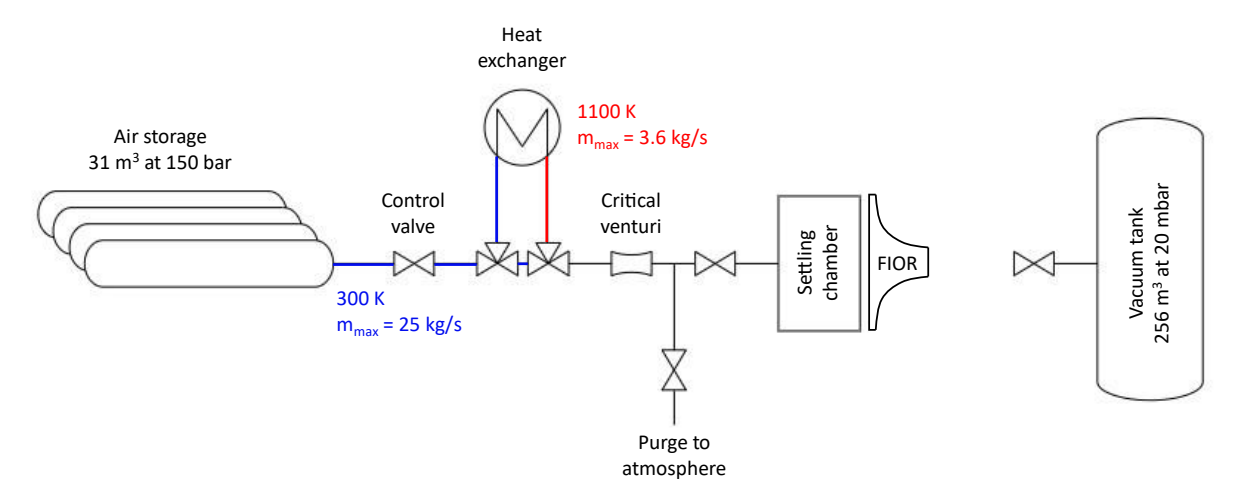


Figure 2: PT1 wind tunnel schematic with the FIOR test section.

A variety of instruments are installed along the wind tunnel and test section to accurately characterize the flow. Up to six Type-K thermocouples (K1X-S304-062-EX-12-MPCX, Evolution Sensors and Controls, LLC) were used upstream of the nozzle for reference temperature measurements. Temperature data is acquired using a 48-Channel precision thermocouple measurement instrument (EX1048, VTI Instruments). Pressure measurements were taken using a pressure scanner (Scanivalve MPS4264) module, which recorded data from two total pressure ports in the settling chamber and 25 static pressure ports along the nozzle wall.

The probe nacelle was mounted downstream of the open jet, secured to an optical table using a hollow rail. This rail allowed to adjust the distance between the probe and the nozzle and to introduce redirecting mirrors inside to help route the laser to the entry port located in the nacelle floor. Coolant air was supplied through a 40 mm diameter hose connected to the rear of the nacelle, with upstream total pressures up to 6 bar, although pressure losses across the coolant venturi reduced the effective pressure to 1.9 bar.

In this study, two test campaigns were performed: the first characterized the vibration levels of the probe under subsonic and underexpanded supersonic jet conditions, and the second demonstrated the laser technique under the measured vibration levels.

2.3. Flow-Induced Vibration Testing

When exposing the nacelle to the free jet flow, vibrations in the nacelle are measured with an accelerometer (4533-B-001, Brüel & Kjaer) that is placed in the location of the upper optical window. The accelerometer was secured using a 3D printed insert, it provides a nominal sensitivity of $51.13 \ mV/ms^2$, a maximum measurable frequency of 12.8 kHz, a maximum range of $\pm 700 \ m/s^2$, and it is connected to a National Instruments card acquiring at 50 kHz. A low-pass filter at the maximum frequency is applied during post processing.

Accelerometer data is directly used to extract frequency domain information, but it is also integrated to retrieve the amplitude and frequencies of the displacements (vibrations). To obtain displacement from the measured acceleration, a double integration is required. Direct integration in the time domain introduces cumulative errors that can strongly distort the signal if not considered. A frequency-domain FFT integration approach mitigates this issue as it removes most of the non-periodic, cumulative error that arises in the time-domain procedure [12]. By applying a Fourier transform, the integration operation becomes a division of the acceleration spectrum by $i2\pi f_n$ as shown in Equation (1). The displacement signal is then reconstructed in the time domain by applying the inverse Fourier transform.

For vibration analysis, the structure oscillates about an equilibrium position without a net displacement. Accordingly, a high-pass filter is applied to suppress residual low-frequency components. In this study, a cut-off frequency of 10 Hz was chosen for the filter. This value is low enough to preserve relevant low frequency components but reducing it more produced unrealistic vibration amplitudes still caused by the integration process. Higher values did not produce a significant change in the signal.

time domain
$$\underbrace{v(t)}_{time \ domain} = \underbrace{\sum_{n=-\infty}^{\infty} C_n e^{i2\pi f_n t}}_{time \ domain} \rightarrow \underbrace{\int y(t)dt}_{time \ domain} = \underbrace{\frac{1}{i2\pi f_n} \sum_{n=-\infty}^{\infty} C_n e^{i2\pi f_n t}}_{time \ domain}$$
(1)

Apart from the accelerometer, a Phantom v2012 high-speed camera was used to record videos of the vibrational response of the nacelle. The frame rate was limited to 20 kHz as higher frequencies implied shorter exposure times and not enough light was captured by the camera sensor. The maximum frequency that can be detected without aliasing errors is 10 kHz. The recordings were processed using the Proper Orthogonal Decomposition (POD) algorithm described by Sieber et al. [13]. This method decomposes the nacelle motion into a linear combination of orthogonal vibration modes ranked according to their energy content. To minimize measurement interference, the camera was mounted in a cantilevered configuration on an isolated optical table, separate from the support structure of the nacelle. The spatial resolution of the recorded images was $0.32 \, mm/pixels$. Figure 3a shows the experimental setup with the optical measurement techniques and Figure 3b shows a detail schematic of the location of the accelerometers and the field of view of the optical measurement techniques.

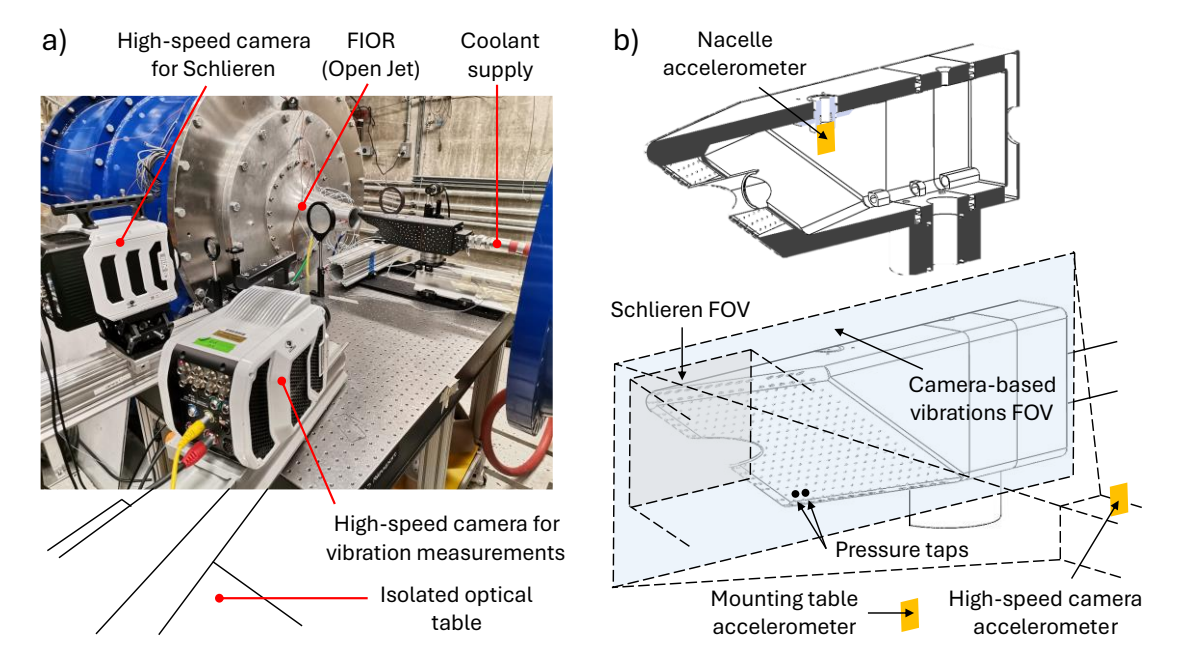


Figure 3: Experimental facility and optical measurement techniques for the vibrations measurement campaign (a), with a schematic of the instrumentation and FOVs (b).

Two additional accelerometers were employed to characterize potential vibration sources external to the probe. One accelerometer was mounted on the optical table supporting the probe, while the other was attached directly to the high-speed camera used for optical vibration measurements. This last accelerometer confirmed that the vibration amplitude of the camera was consistently at least two orders of magnitude lower than that of the probe. This result verifies that the camera was properly isolated from the facility and that the vibration captured in the videos is attributable solely to the probe dynamics.

A generic cold-flow test sequence representative of the tests performed in the accelerometer campaign is shown in Figure 4. The coolant pressure is first increased in an intervallic manner to acquire vibrations data just due to coolant blowing and once a value of $P_{0c}=1.8\ bar$ is reached, the fast-actuating valve is opened to perform sudden blowdowns through FIOR at total pressures ranging between $1.37 < P_{01} < 2.7$ bar. This enables the acquisition of vibration data due to both coolant and Open Jet effects. Figure 4 also shows example accelerometer data after the double integration process for one Mach number setpoint.

HiSST-2025-279 Page |

5

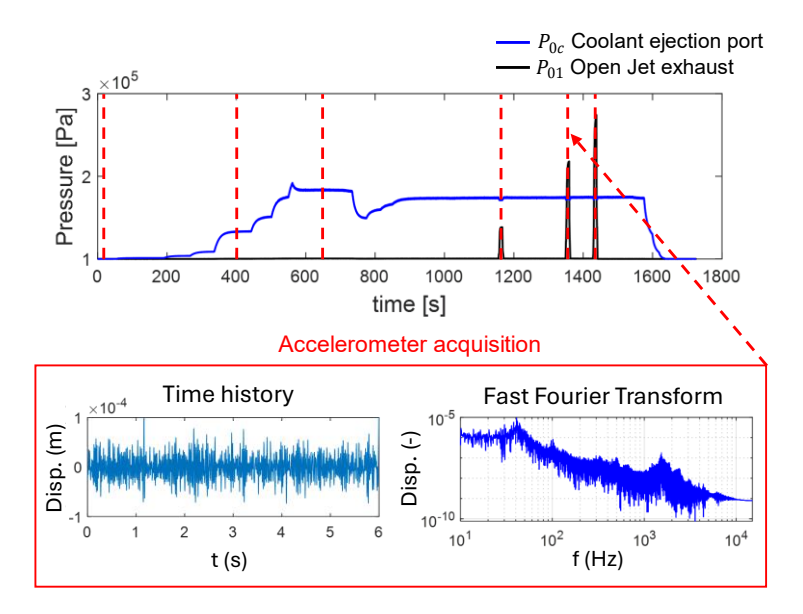


Figure 4: Total pressure traces in the Open Jet and the coolant ejection holes during the test alongside the accelerometer acquisition periods.

2.4. Laser-Based Flow Visualization

A 532 nm continuous-wave laser (Dantec Dynamics FiberFlow System) with a maximum output power of 1 W was used as the illumination source. The beam was routed into the probe through the bottom using a series of plane mirrors. Inside the probe, the beam was shaped into a laser sheet using an optical train consisting of a 45° steering mirror, a spherical converging lens (f = 400 mm), and a cylindrical lens (f = -15 mm). The spherical lens locates the beam waist, corresponding to the thinnest section of the laser sheet, 200 mm away from the tip of the probe. The probe tip was positioned 240 mm from the nozzle exit so that the beam waist intersected the flow approximately 40 mm downstream of the nozzle. The width of the sheet within the region of interest ranged between 40 and 55 mm.

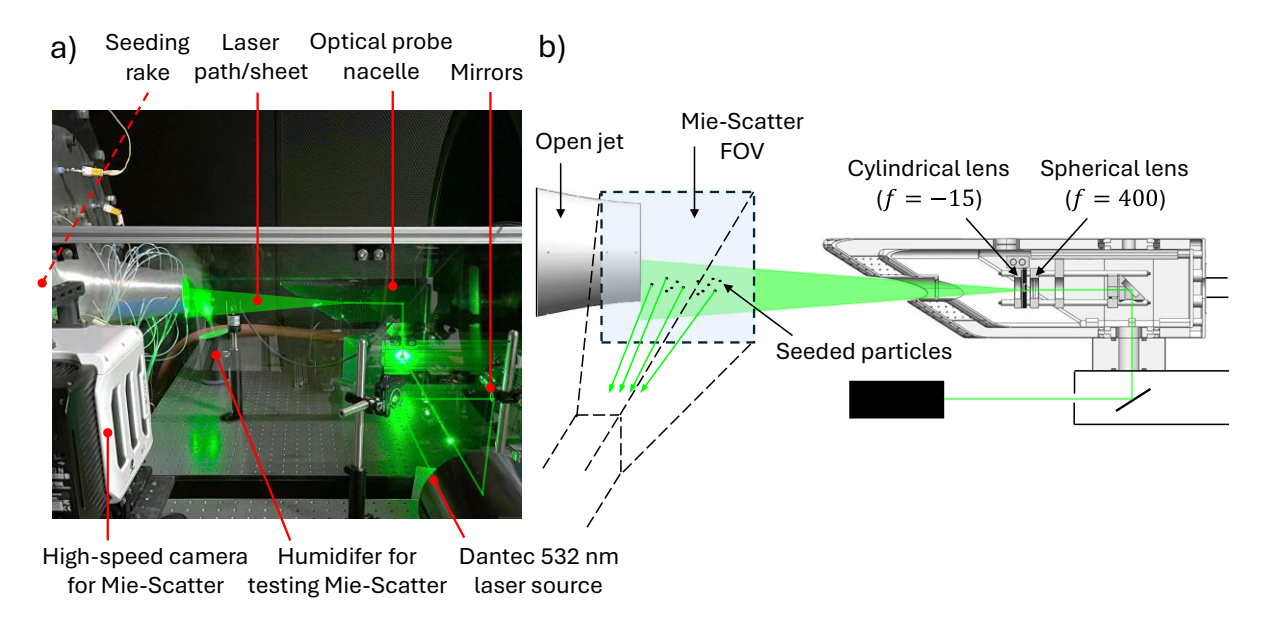


Figure 5: Experimental facility and optical measurement techniques for the laser technique campaign (a), with a schematic of the instrumentation and FOVs (b).

To enable flow visualization, the laser light was scattered by micron-sized oil droplets introduced into the test section. The droplets were generated using a ViCount 5000 smoke generator operated with Smoke Oil Type 180 and delivered through a seeding rake installed in the settling chamber. The rake

geometry was designed to preferentially seed the lower portion of the nozzle exit, thereby concentrating tracer particles in the region of interest. The height of the probe was adjust accordingly to deliver the Laser sheet to the lower half of the nozzle.

Scattered light was recorded using a Phantom TMX 5010 high-speed camera at acquisition frequencies between 5 and 20 kHz. The maximum allowable exposure time was selected for each frame rate to maximize light collection by the camera sensor, although this introduced a degree of motion blur at the higher acquisition rates. Figure 5a shows the experimental setup with the optical measurement techniques and Figure 5b shows a detail schematic of the internal and external laser path, and the Mie-Scattering mechanism achieved by illuminating the oil droplets.

For all the tests conducted in the laser-based visualization campaign, the coolant pressure upstream the venturi was kept at 6 bar (maximum level reached in the vibrations campaign), and the total pressure of the open jet was varied in an intervallic manner from 1.01 to 2 bar to reach Mach number setpoints between 0.15 and underexpanded conditions (Mach 1.05).

3. Results

3.1. Accelerometer-Based Vibrations

The acceleration signal of the nacelle for all the tests is integrated as explained in Section 2.3. To extract an average value of the peak-to-peak displacement at every condition; first, an interpolation code is run that bounds the displacement amplitude signal in the upper and lower part generating an approximated envelope; second, a peak-detection algorithm is run that detects the peak of the envelopes; and finally, the maximum displacement bounds are generated by averaging the 5 largest peaks of each envelope. Figure 6a shows the original signal, with the interpolated envelopes and the maximum displacement bounds, also known as the peak-to-peak displacement.

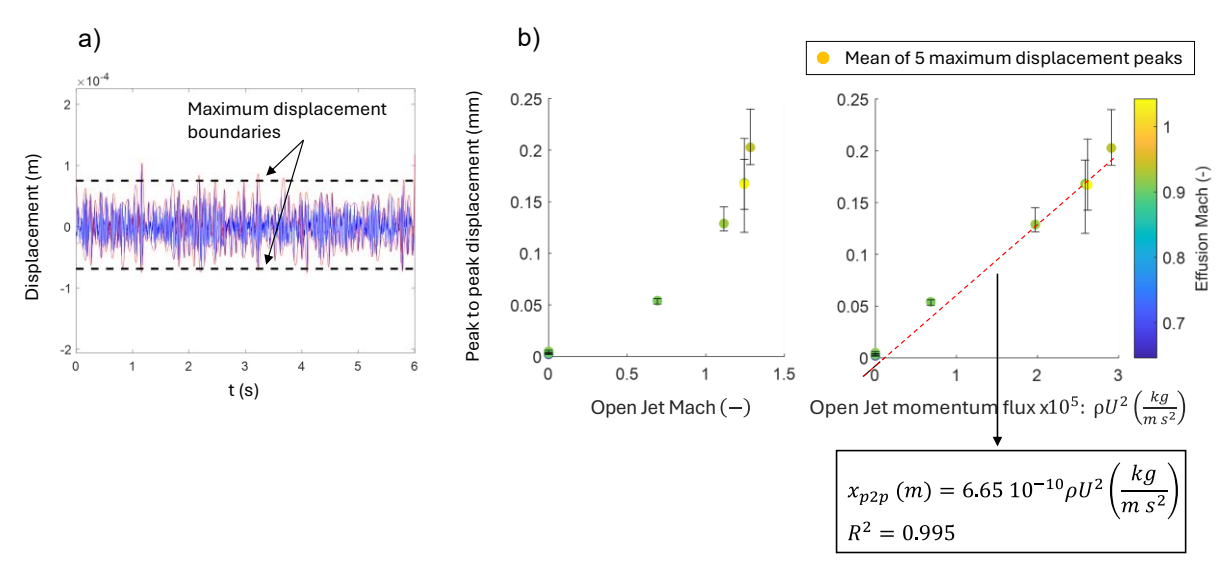


Figure 6: Envelope of peak-to-peak vibration amplitude (a) and relationship between the vibration amplitude and the flow conditions through the open jet (c)

In order to correlate the peak-to-peak vibrations with the conditions of the free Jet, different scaling parameters have been tried. Figure 6b shows scatterplots of the peak-to-peak displacement with respect to the exhaust Mach number and the momentum flux of the free jet for different coolant Mach numbers at the ejection holes.

First, the results indicate that coolant flow does not significantly influence the overall vibration response. Therefore, operating the probe in hotter environments that require higher coolant pressures is not expected to adversely affect the vibration levels or the stability of the optical system.

Vibrations increase noticeably with the Mach number of the Open Jet, but they do it nonlinearly as the Mach number is not completely representative of the energy of the jet. The momentum flux (ρU^2) ,

however, is a more representative variable of the kinetic energy of the jet $\left(\frac{1}{2}\rho U^2\right)$. It is found that there is a linear correlation between the vibrations of the nacelle and the momentum flux of the Open Jet. A linear fit is extracted with an R^2 value of 0.995 that can be used to estimate the peak-to-peak vibrations experienced by the nacelle exposed to a free jet at a given momentum flux prior to testing and help to understand its effect on the optics. At a maximum Mach number of 1.15, the peak-to-peak displacement measured is 0.21 mm.

The acceleration signal is transformed into the frequency domain via an FFT and the frequency with the highest energy content is extracted for all the conditions studied. Figure 7 shows the frequencies that dominate the acceleration and the displacement signal of the probe depending on Mach number. Figure 7 shows two dominant frequencies in the response, a high frequency at $f_{high}=1577.7~Hz$ and a low frequency at $f_{low}=45.1~Hz$. The acceleration signal is dominated by the high frequency component, but the displacement is dominated by the low frequency mode as displacement cannot adapt immediately to a high-frequency change in acceleration. This behavior can also be explained by looking at the integration process, as integrating a signal (dividing by $i2\pi f_n$) inherently increases the content of the lower frequencies relative to the higher ones.

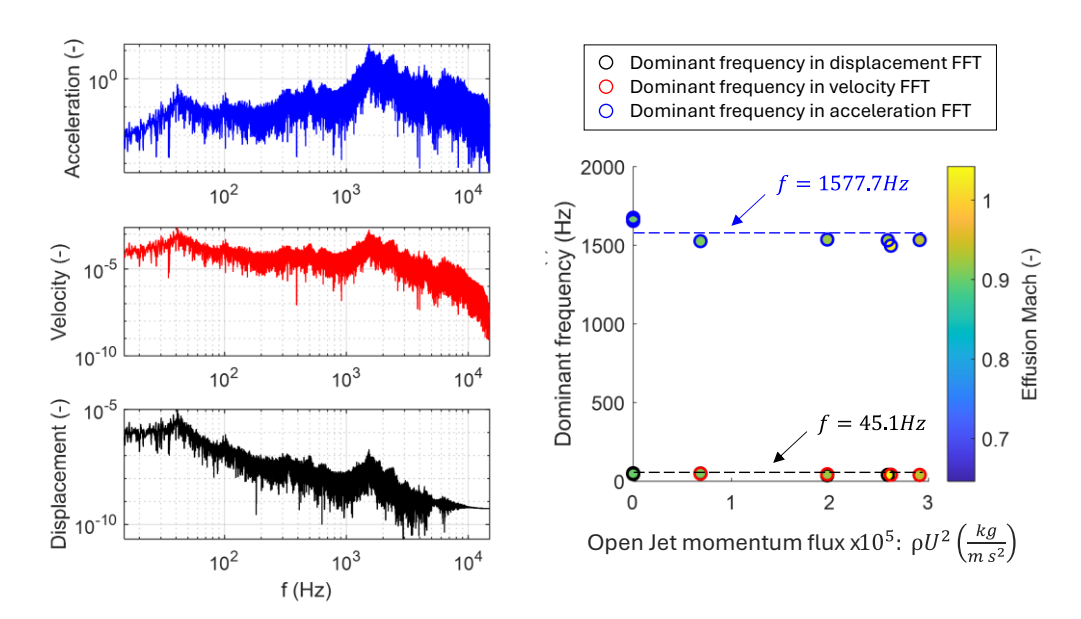


Figure 7: FFT of acceleration, velocity and displacement signal and dominant frequency of each signal for different open jet momentum fluxes.

3.2. Uncertainty Quantification

A calibration chart is provided by Brüel & Kjaer giving a nominal sensitivity for the accelerometers of $s_n=10.28 \left(mV/(ms^2)\right)\pm 8\%$ inside the 0-12.8kHz frequency range, which is used for the conversion between voltage and acceleration. The uncertainty of the peak-to-peak displacement has been computed using the sensitivity analysis proposed by Moffat [14] in which the independent variables (accelerometer sensitivity) are varied within their uncertainty bands and the change produced in the dependent variables (peak-to-peak vibration) is propagated. The uncertainties in peak-to-peak displacement are included in Figure 6 for all the experimental values.

3.3. Camera-Based Vibrations

Camera-based vibration measurements were used to verify the accelerometer results and confirm that the double integration process did not introduce significant errors. Proper Orthogonal Decomposition (POD) is well suited to identify coherent mode structures in unsteady flows. However, in this case the recordings were nearly steady due to the low vibration amplitude of the probe. As a result, the energy of the dominant modes was only slightly higher than the background noise of the images, and in some cases lower than the noise produced by instrumentation wires moving across the FOV with the flow. The third-highest energy mode was the first associated with the vertical motion of the nacelle, as shown

in Figure 8a. The shape of the mode is displayed, where the color shifts indicate changes in the light intensity captured by the sensor. These variations occur because the nacelle moves up and down, altering the background intensity received by the affected pixels.

Figure 8b shows the frequency content of this spatial mode. The temporal coefficient exhibits a clear oscillatory pattern, and its FFT indicates a dominant frequency at 45 Hz. This matches the frequency identified by the accelerometer after the double integration. The agreement confirms that the accelerometer results are reliable as the mode shape extracted by POD at this frequency clearly shows an oscillating motion. The vertical color shifts shown in Figure 8a affect one row of pixels. This resolution is not sufficient to resolve the true vibration amplitude, but it bounds it to be less than 0.32 mm (pixel size), which is consistent with the accelerometer measurements.

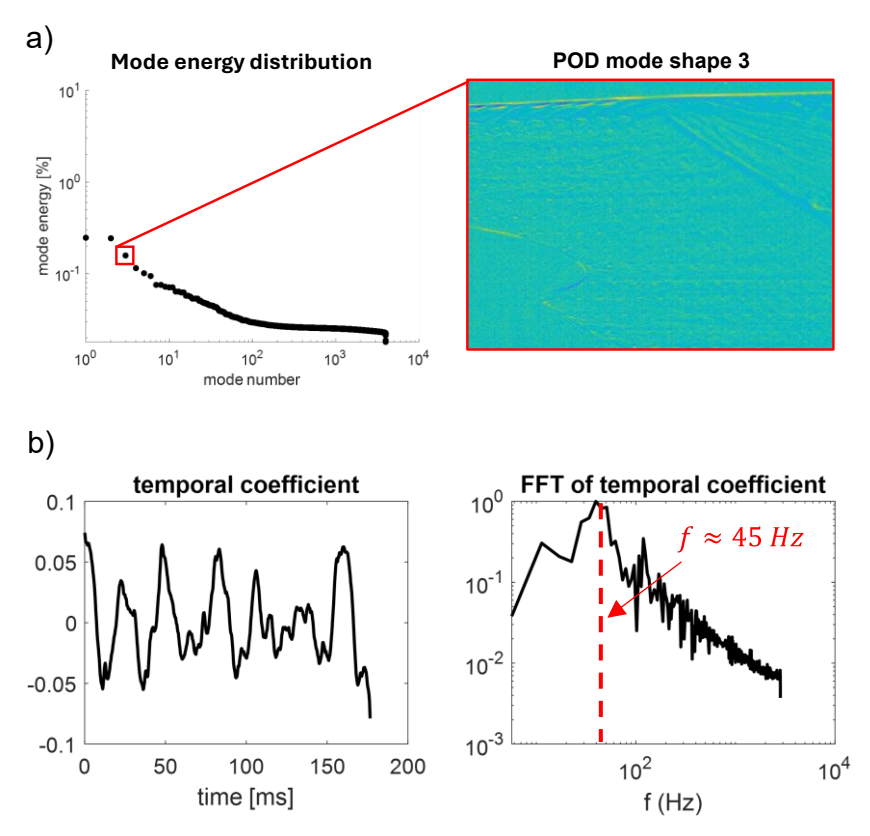


Figure 8: Mode energy distribution, mode shape (a), and time history and FFT of the temporal coefficient for the mode associated with the vertical motion of the nacelle (b)

The first campaign quantified nacelle vibrations under open-jet flow, with a maximum amplitude of 0.21 mm measured at the upper optical window at Mach 1.05 and a dominant frequency of 45 Hz. The second campaign, presented in the next sections assess the performance of the laser-based technique under the same conditions to verify that nacelle vibrations did not compromise the measurement technique.

3.4. Flow Visualization

Images of the seeded flow were recorded using the Phantom high-speed camera while the particles were illuminated by the laser sheet delivered through the nacelle. Higher-quality visualizations were obtained at lower Mach numbers (0.15 and 0.5) due to the longer particle residence time within the field of view and the higher particle concentration, which increased the scattered light intensity. At higher Mach numbers (0.7 and underexpanded), the reduced residence time and lower particle concentration decreased the scattered light intensity, resulting in a lower signal-to-noise ratio. For all conditions, the laser sheet was delivered uninterruptedly, showcasing the effectiveness of the approach for all the vibrations levels experienced in the free jet facility up to underexpanded conditions.

Figure 9 presents four snapshots at different Mach numbers, along with a scaled schematic of the FIOR facility to indicate the location of the field of view relative to the test nozzle. The cases shown correspond to Mach 0.15, 0.5, 0.7, and 1.0 (underexpanded). A frame rate of 10 kHz with the maximum allowable exposure time (99.7 μ s) was used for all conditions, except at Mach 0.15 where a higher frame rate of 15 kHz and a shorter exposure time of 66.4 μ s could be applied while maintaining sufficient signal intensity.

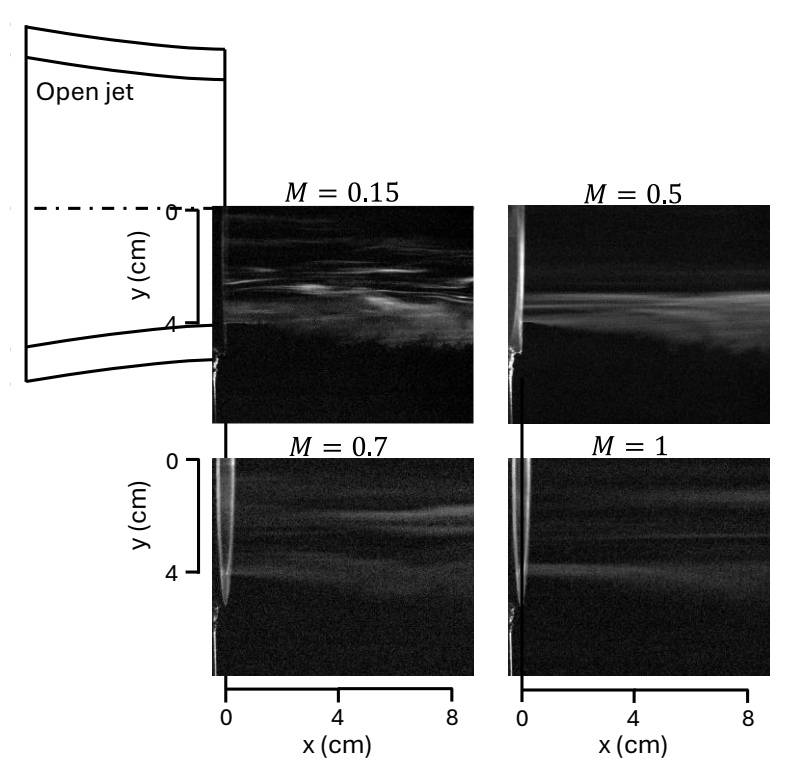


Figure 9: Raw Images at Mach 0.15 (a), 0.5 (b), 0.7 (c) and underexpanded (d).

3.5. Identification of structures

Using the raw Mie-scatter images, characteristic flow structures within the shear layer of the free jet were identified, serving both to validate the canonical behavior of the FIOR facility at subsonic conditions and to demonstrate the capability of the probe-based optical approach. At the nozzle exit, the jet was observed to remain uniform and homogeneous before entraining the surrounding quiescent air. This interaction initiated a turbulent shear layer that thickened with downstream distance and simultaneously reduced the extent of the potential core, consistent with the schematic in Figure 10a adapted from Strangfeld et al. [15]. These canonical features were clearly visible in all subsonic test cases.

Representative examples of the identified structures are presented in Figure 10b for Mach 0.15, 0.5, and 0.7. In each case, the highlighted arrow tracks shear layer structure originating from Kelvin–Helmholtz instabilities and convecting downstream with the mean jet flow. The structures increase in scale with axial distance, reflecting the progressive entrainment of both surrounding air and core flow into the shear layer. For higher Mach numbers, the signal intensity was not sufficient to clearly identify flow structures within the shear layer as most of the seeded particles remained within the core.

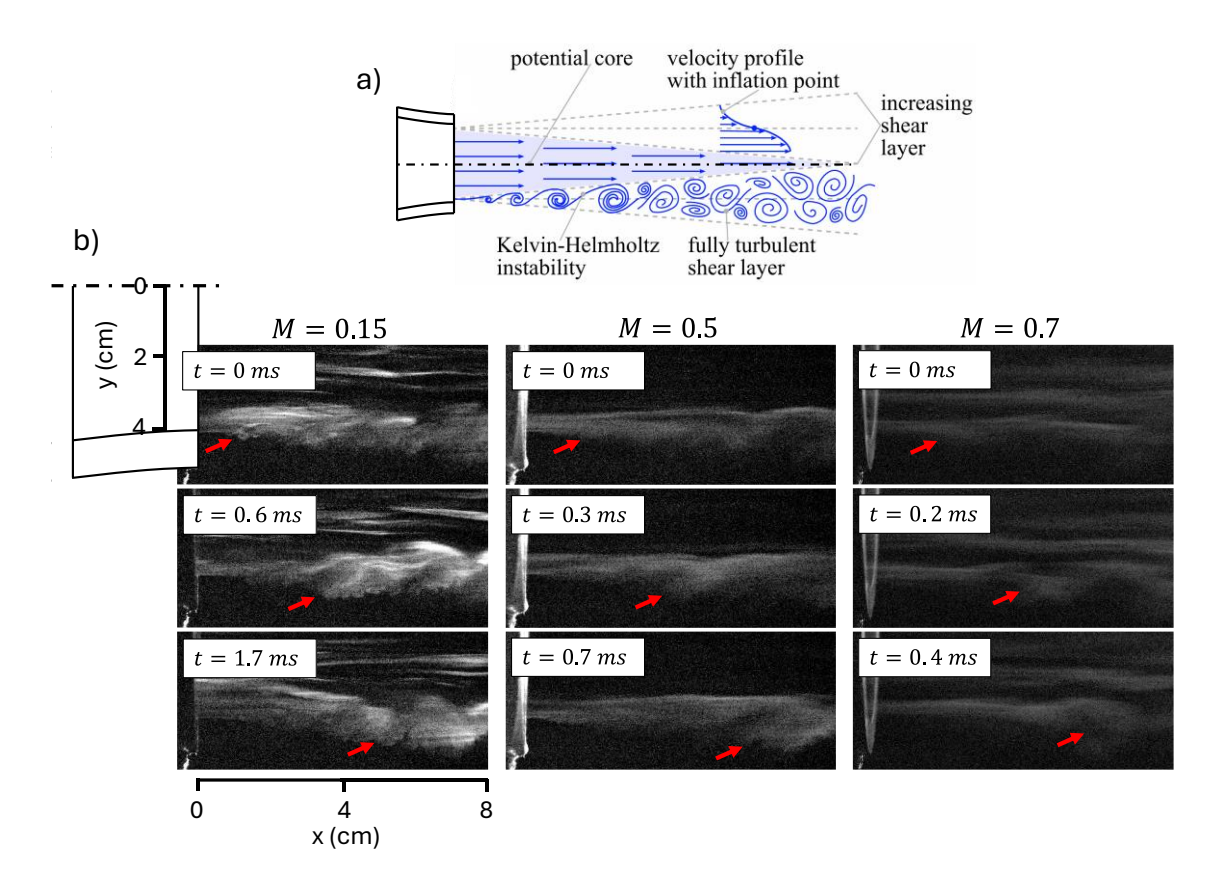


Figure 10: Schematic of a subsonic free jet flow topology, reproduced from [15] (a) and identified shear layer structures developing in time at Mach 0.15, 0.5, and 0.7 (b).

3.6. Determination of the average jet plume velocity

This section addresses the extraction of quantitative data from the Mie-scatter recordings. The quality of the acquired images was not temporally uniform, with some sequences exhibiting high seeding concentrations and others showing sparse or non-uniform particle distributions. For this reason, the use of conventional PIV algorithms yielded inconsistent velocity fields. Instead, the analysis was performed on selected frames where particle motion across the field of view was clearly visible. In these frames, the displacement of particle clusters was quantified by tracking the maximum pixel intensity of the clusters, and the corresponding velocity was obtained applying a spatial and temporal calibration. This procedure was applied to clusters crossing the averaging window indicated in Figure 11a, which spans a radial distance of 2 cm from the nozzle centerline and an axial distance of 4–8 cm downstream. Regions closer to the nozzle were excluded to minimize the influence of lagged particles. For each Mach number, 50 instantaneous velocity values were extracted and subsequently averaged to determine the mean velocity in the region of interest. The resulting values were compared to the Mach numbers inferred from pressure data, as shown in Figure 11b. The uncertainty bands in the plot represent the stochastic variation of the 50 measurements, modelled with a normal distribution, where the standard deviation defines the uncertainty bounds.

This analysis not only demonstrates that the probe consistently delivered the laser sheet under all vibration conditions and Mach numbers tested but also uses the Mie-scatter technique as an average velocity diagnostic. The optically derived velocities closely follow the ideal line defined by the pressure-based Mach numbers. Deviations increase with Mach number, accompanied by larger uncertainty bands, which is attributed to the reduced video quality at higher flow speeds and to the finite particle response time required to adapt to the free-stream velocity.

HiSST-2025-279

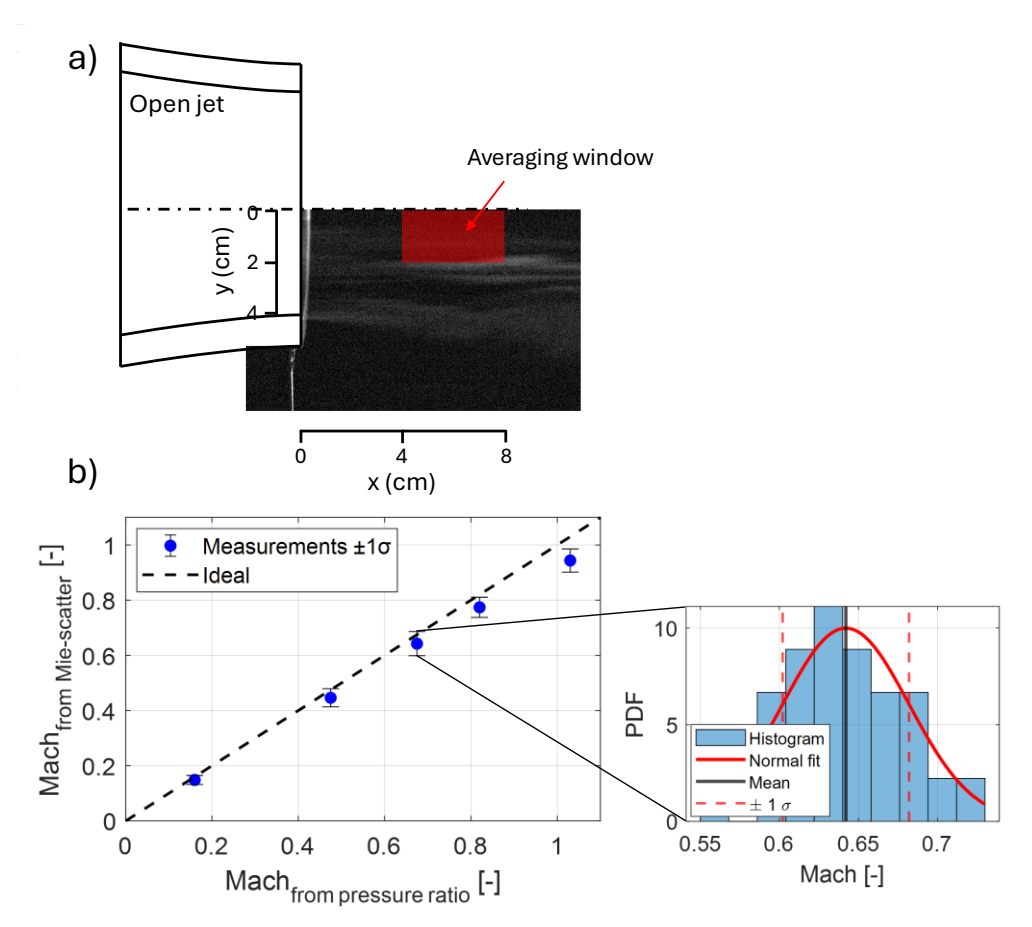


Figure 11: Region for averaging Mie-scattered velocity data (a), and a comparison of the pressure-derived Mach number with the optically measured one with error bands representing the stochastic uncertainty (b).

4. Conclusions

This study has evaluated the performance of an in-flow optical probe nacelle under flow-induced vibrations and demonstrated its ability to deliver laser diagnostics in a supersonic open-jet facility. The central objective was to verify that probe vibrations did not compromise laser sheet stability or the quality of the optical measurements.

Two experimental campaigns were carried out in the Facility for Instrumentation and Open-Jet Research (FIOR). The first campaign characterized nacelle vibrations across a range of subsonic and supersonic jet conditions. Vibrations increased linearly with jet momentum flux, reaching a maximum amplitude of 0.21 mm at Mach 1.15. Frequency analysis revealed that accelerations were dominated by a high-frequency (\approx 1600 Hz) mode, while displacements were governed by a lower-frequency (\approx 45 Hz) mode. The response was confirmed through both accelerometer measurements and high-speed optical imaging. Coolant flow did not significantly influence the vibration response, demonstrating that probe operation at higher coolant pressures—required in hot environments—does not add a detrimental effect to optical stability.

The second campaign integrated planar Mie scattering within the probe to evaluate optical performance under the measured vibration levels. Results demonstrated uninterrupted delivery of the laser sheet across all tested Mach numbers, with successful visualization of flow structures up to underexpanded conditions. Quantitative velocity estimates obtained by tracking particle clusters showed close agreement with Mach numbers inferred from pressure data, validating the measurement approach. At higher Mach numbers, deviations increased due to reduced seeding quality and finite particle response time, but the probe maintained stable optical performance under all conditions.

Overall, this study establishes that in-flow optical delivery is viable under the vibration environment of supersonic open-jet flows. The actively cooled probe nacelle enables laser sheet formation with minimal

degradation of alignment or signal quality. These findings represent a step toward optical probes capable of supporting advanced diagnostics within supersonic facilities.

References

- [1] D. L. Goldstein and R. Scherrer, "Design and calibration of a total-temperature probe for use at supersonic speeds," 1949.
- [2] A. R. Porro, "Pressure probe designs for dynamic pressure measurements in a supersonic flow field," in *ICIASF 2001 Record, 19th International Congress on Instrumentation in Aerospace Simulation Facilities (Cat. No. 01CH37215)*, IEEE, 2001, pp. 417–426.
- [3] L. Jiang, S. Manipurath, G. Bourque, and M. Houde, "Flow field of a triple-walled gas-sampling probe with sub-cooled boiling effect," *Flow Measurement and Instrumentation*, vol. 18, no. 3–4, pp. 156–165, 2007.
- [4] J.-F. Brouckaert, M. Mersinligil, and M. Pau, "A Conceptual Design Study for a New High Temperature Fast Response Cooled Total Pressure Probe," *J Eng Gas Turbine Power*, vol. 131, no. 2, Dec. 2008, doi: 10.1115/1.2969092.
- [5] N. T. Lagen and J. M. Seiner, "Evaluation of water cooled supersonic temperature and pressure probes for application to 2000 F flows," in *36th International Instrumentation Symposium*, 1990, p. 6.
- [6] M. J. Won, "Cone-Probe Rake Design and Calibration for Supersonic Wind Tunnel Models," 1999.
- [7] J. M. Fisher, "Advancements and Practical Applications of Molecular Tagging Velocimetry in Hypersonic Flows," PhD Dissertation, Purdue University, West Lafayette, 2020.
- [8] B. A. Segall, D. Shekhtman, A. Hameed, J. H. Chen, and N. J. Parziale, "Profiles of streamwise velocity and fluctuations in a hypersonic turbulent boundary layer using acetone tagging velocimetry," *Exp Fluids*, vol. 64, no. 6, p. 122, 2023.
- [9] I. Lasala Aza *et al.*, "Numerical assessment of an aerodynamic probe to enable short focal length laser diagnostics in high temperature supersonic flows based on flow disturbance," *J Turbomach*, pp. 1–23, Dec. 2024, doi: 10.1115/1.4067379.
- [10] J. A. Inman *et al.*, "Nitric-oxide planar laser-induced fluorescence measurements in the hypersonic materials environmental test system," *AIAA journal*, vol. 51, no. 10, pp. 2365–2379, 2013
- [11] G. Paniagua *et al.*, "Design of the Purdue experimental turbine aerothermal laboratory for optical and surface aerothermal measurements," *J Eng Gas Turbine Power*, vol. 141, no. 1, p. 012601, 2019.
- [12] R. Brincker and A. Brandt, "FFT Integration of Time Series using an Overlap-Add Technique," in *Structural Dynamics, Volume 3: Proceedings of the 28th IMAC, A Conference on Structural Dynamics, 2010*, Springer, 2011, pp. 1467–1474.
- [13] M. Sieber, C. O. Paschereit, and K. Oberleithner, "Spectral proper orthogonal decomposition," *J Fluid Mech*, vol. 792, pp. 798–828, 2016.
- [14] R. J. Moffat, "Using uncertainty analysis in the planning of an experiment," ASME. J. Fluids Eng., vol. 107, no. 2, pp. 173–178, 1985.
- [15] C. Strangfeld, B. Grotelüschen, and B. Bühling, "Air-Coupled Broadband Impact-Echo Actuation Using Supersonic Jet Flow," *J Nondestr Eval*, vol. 43, no. 2, p. 45, 2024.

HiSST-2025-279